Ondra, V., & Titurus, B. (2019). Theoretical and experimental modal analysis of a beam-tendon system. *Mechanical Systems and Signal Processing*, *132*, 55-71. https://doi.org/10.1016/j.ymssp.2019.06.016

Theoretical and experimental modal analysis of a beam-tendon system

V. Ondra[a,*], B. Titurus[a]

[a] *University of Bristol, Department of Aerospace Engineering, University Walk, BS8 1TR Bristol, United Kingdom*

Abstract

Theoretical and experimental modal analysis of the system consisting of the Euler-Bernoulli beam axially loaded by a tendon is studied in the paper. The beam-tendon system is modelled using a set of partial differential equations derived by Hamilton's principle and the coupling between the beam and the tendon is ensured by the boundary conditions. Theoretical modal analysis is conducted using a boundary value problem solver and the results are thoroughly experimentally validated using a bench-top experiment. In particular, the effect of the tendon tension on the modal properties of the system is studied. It is found that by increasing the tension, the natural frequencies of the beam decrease while the natural frequencies of the tendon increase. It is also shown that these two sets of modes interact with each other through frequency loci veering. The effect of the tendon mass is also experimentally and numerically studied and it is shown that lighter tendon produces fewer vibration modes in the studied frequency region. Two further numerical studies are conducted to demonstrate the effect of the tendon on the torsional modes of the beam, and to study the structural stability. Overall, an excellent agreement between the numerical and experimental results is obtained, giving the confidence in the derived theoretical model.

Keywords: beam-tendon system, theoretical and experimental modal analysis, Euler-Bernoulli beam, frequency loci veering, Hamilton's principle

Highlights

- A system consisting of the Euler-Bernoulli beam subjected to tendon-induced axial loading is studied
- The system is modelled using a set of partial differential equations derived by Hamilton's principle
- The model is thoroughly experimentally validated for a wide range of loadings and configurations
- The effect of the tendon tension and its mass on the modal properties and frequency loci veering are studied
- Further numerical studies show the effect of the tendon on the torsional modes and structural stability

Nomenclature

Symbol	Description
A	Area of the cross-section, m^2
f	Natural frequency, Hz
f^{exp}	Experimentally obtained natural frequency, Hz
f^{nom}	Natural frequencies computed using nominal parameters, Hz

*Corresponding author.
Email addresses: vaclav.ondra@bristol.ac.uk (V. Ondra), brano.titurus@bristol.ac.uk (B. Titurus)

f^{upd}	Natural frequencies computed using updated parameters, Hz
f^{com}	Natural frequencies computed for beam with tip mass, Hz
F_v, F_w	External excitation forces in y and z directions, N
g	Gravitational acceleration, $9.81\,\mathrm{m\,s^{-2}}$
E	Young's modulus of elasticity, Pa
G	Shear modulus of elasticity, Pa
I_o	Polar moment of inertia of the cross-section, m^4
I_y, I_z	Moments of inertia of the cross-section about y and z axis, m^4
J	Torsional constant, m^4
L	Length of the beam and tendon, m
m	Mass of the blade per unit length, $\mathrm{kg\,m^{-1}}$
m_{t}	Mass of the tendon per unit length, $\mathrm{kg\,m^{-1}}$
M_{L}	Weight placed on the hanging platform, kg
M_{tip}	Tip mass, kg
N_m	Number of vibration modes
P	Applied tension corresponding to axial force, N
P_{cr}	Critical force, N
Q_ϕ	External excitation moment about neutral axis (torque), N m
t	Time, s
T	Kinetic energy, J
U	Potential energy, J
v, w	Bending displacements of beam in y and z directions, m
v_{t}, w_{t}	Transversal displacements of tendon in y and z directions, m
δW	Virtual work, J
$W, V, \Phi, W_{\mathrm{t}}, V_{\mathrm{t}}$	Mode shape components of beam and tendon system
x	Independent spatial variable, m
iV, iW	i-th mode in y and z direction
y, z	Coordinate axes in the plane of the cross-section
ζ	Damping ratio, %
ϕ	Torsional displacement, rad
ω	Angular frequency, $\mathrm{rad\,s^{-1}}$
Ψ	Mode shape of the system
$\mathrm{std}(\bullet)$	Standard deviation
$\dot{(\bullet)}$	Partial derivative with respect to time
$(\bullet)'$	Partial derivative with respect to spatial variable
BC	Boundary condition
FRF	Frequency response function
LSCF	Least-square complex frequency estimator
F-L	Frequency-loading
MAC	Modal assurance criteria
ODE	Ordinary differential equation
PDE	Partial differential equation

1. Introduction

Free vibration of beams and tendons (cables, strings) have been extensively studied, because they are two essential structural elements that are frequently used in many engineering applications. There is an overwhelming number of studies that focus on different aspects of beam and string modelling, application and testing. Many review papers and monographs have been written on the topic [1–4]. Often, the beam models are augmented to suit a particular application. For instance, beam models with pretension and under an action of a moving mass [5] are used as models of rail road tracks, bridges or machining processes, while the rotating composite beams are of interest in aerospace engineering where they represent rotorcraft

blades [6]. A number of studies also investigated vibration of axially loaded beams [7] and their stability [8, 9]. Tendons have also been used in a number of applications, often as actuators or a means of vibration control. A comprehensive review of active tendon control can be found in [10, 11]. The beams and tendons are almost always used and modelled separately. In contrast, a coupled system that consists of a cantilever beam of a box cross-section that is axially loaded by a tendon that passes through the body of the beam is studied in this paper.

A few studies used a similar configuration to the present one, i.e. a beam-like structure loaded by a tendon. In [12–14] an externally connected tendon was used for vibration control of a cantilever beam. It was found that vibration energy of the beam in a prescribed frequency range can be removed by applying and releasing the tension in a specific manner, thereby effectively suppressing the vibration of the beam. These studies mainly focused on the control aspects of the problem, but the modelling of the dynamic response was also performed using the Euler-Bernoulli beam theory and the presence of the tendon was accounted for by an axial force, i.e. the motion of the tendon was not modelled. The axially loaded beam models were considered in the previous studies, presumably because the dynamics of such axially loaded beams has been well understood [7–9]. A string-beam system has been used as a representation of optic cable coupler in [15] and its bifurcation and chaotic dynamics mathematical investigated in [16]. In these studies, the axial tension of the string had no influence on the beam since there was no direct coupling between them. The use of string that is mounted inside a helicopter tail boom for response suppression was numerically and experimentally explored in [17]. Unlike in the previous studies, the system was modelled using the finite element method. It was shown that the cable can be tuned as a vibration absorber which not only positions an antiresonance at the excitation frequency for a critical location on the primary structure, but also shifts the natural frequencies of the system. The interaction between the primary structure and the cable in terms of eigenvalue loci veering was observed and will be observed also in the case of the beam-tendon system studied herein. In this paper, a beam subjected to tendon-induced axial loading is studied. It was suggested in [18, 19] that the tension of the tendon that is incorporated in a slender structure can be used to adjust the structure's dynamic properties, thereby providing a control authority necessary for vibration mitigation. This can be used, for example, as a means of resonance avoidance in rotorcraft [20] or any other slender structure.

The objective of this paper is to study the free vibration on a beam-tendon system. The present study extends [18, 19] by presenting the detailed derivation of the equations of motion and boundary conditions of the system, and by performing thorough experimental validation for a wide range of loadings and configurations. To the best knowledge of the authors, the means of modelling used in the paper and experimental validation has not yet been reported in literature. The paper is organised as follows: in section 2 the theoretical model of the system is derived using Hamilton's principle and the numerical procedure used to obtain the modal properties is described. The theoretical model is experimentally validated in section 3. Firstly, the underlying beam model (without the tendon or axial load) is obtained using the model updating in section 3.2. Then, the validation of the beam-tendon system is conducted in section 3.3 by means of the comparison of the computed and experimentally measured frequency-loading (F-L) diagrams which show the variation of the natural frequencies with the applied loading. The veering is studied in more detail in section 3.4, and the effect of the tendon mass is investigated in section 3.5. Having validated the model experimentally, two numerical studies that go beyond the experiment's capabilities are performed in section 4. Specifically, in section 4.1 the effect of the tendon on the natural frequency of the torsional mode is studied, and the structural stability of the beam-tendon system is investigated in section 4.2. In section 5 the main findings are summarised, the assumptions and limitations of the theoretical model are discussed, and a practical application of the beam-tendon system is suggested.

2. Theoretical model

The system under consideration is a straight cantilever beam with a box cross-section which is axially loaded by a tendon. The tendon is attached to the beam's tip, passes through its whole body (coincides with the neutral axis) and is clamped at the same location as the beam. A rigid plate tip which serves as a tendon attachment point is located at the free end of the beam as shown in Fig. 1 and seen in the

experimental set-up in Fig. 2. The x axis coincides with the neutral axis of the beam while the y and z axes

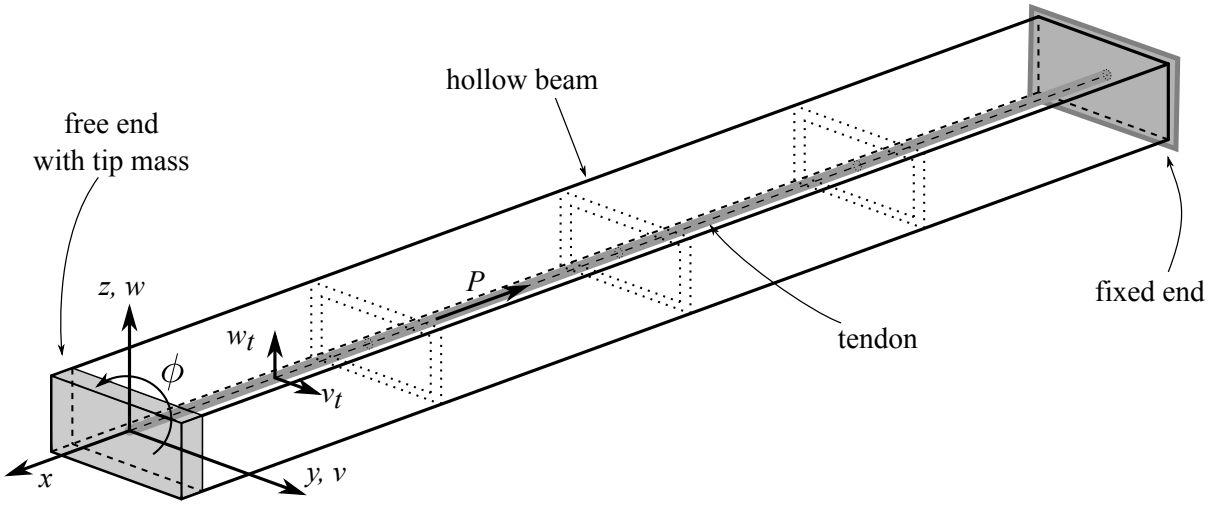

Figure 1: The beam-tendon system studied

lie in the plane of the cross-section. The displacements of the beam in the z and y direction are represented by $w(t,x)$ and $v(t,x)$, respectively, and the rotation of the cross-section about x axis is given by $\phi(t,x)$. The transversal displacements of the tendon in the z and y directions are given $w_{\mathrm{t}}(t,x)$ and $v_{\mathrm{t}}(t,x)$, respectively. The displacement of the tendon is generally different from that of the beam, except for the tip where they are the same. The tendon is loaded by a constant tension P that in turn acts as an axial force applied at the tip of the beam. The tip mass is considered perfectly rigid so its deflections do not affect the tendon tension. Although the external loading is not required for the modal analysis, for the derivation of the theoretical model it is assumed that the beam is excited by the time-varying forces $F_w(t,x)$ and $F_v(t,x)$ in the z and y directions, respectively, and by the torsional moment Q_ϕ about the neutral axis. Since the tendon is fully contained inside the hollow beam, it is not directly externally loaded, but its motion is excited through the interaction with the beam at the tip. The motions of the beam in different directions are not coupled to each other or to the rotation of the cross-section since there is no initial pre-twist and the cross-section is symmetric. The beam and the tendon are assumed to be made of isotropic material that can be described by linear elasticity laws.

For the derivation of governing equations, small deflections and rotations are assumed so that the axial load P acting on the beam remains parallel to its initial direction. Since the derivation is based on the Euler-Bernoulli theory, it is assumed that an infinitely rigid planar cross-section remains planar and normal to the neutral axis after the deformation, and the transverse shear deformation, rotary inertia effects and warping are neglected. It is also assumed that the cross-sectional area of the tendon remains unchanged after the deformation.

2.1. Derivation of the equations of motion and boundary conditions

The equations of motion describing the system and the corresponding boundary conditions (BCs) are derived using Hamilton's principle stated as

$$\int_{t_1}^{t_2} [\delta(U-T) - \delta W]\,\mathrm{d}t = 0 \tag{1}$$

where U is the potential energy, T is the kinetic energy, δW the virtual work of the non-conservative forces and t_1, t_2 are two distinct, arbitrary times [1].

The total potential energy U of the system is given by

$$U = \underbrace{\frac{1}{2}\int_0^L \left(EI_z w''^2 + EI_y v''^2 + GJ\phi'^2\right) \mathrm{d}x}_{U_B} - \underbrace{\frac{1}{2}\int_0^L P\left(w'^2 + v'^2 + \frac{I_o}{A}\phi'^2\right) \mathrm{d}x}_{U_P} + \underbrace{\frac{1}{2}\int_0^L P\left(w_t'^2 + v_t'^2\right) \mathrm{d}x}_{U_t}, \tag{2}$$

where U_B is the strain energy of the beam given by the Euler-Bernoulli theory [1], U_P is the potential energy associated with the tendon-induced axial force [7], U_t is the potential energy stored in the tendon [4], E is Young's modulus of elasticity, I_z and I_y are the moments of inertia of the cross-section about the y and z axis, respectively, G is the shear modulus of elasticity, J is the torsional constant, A is the area of the cross-section, I_o is the polar moment of inertia of the cross-section, and $()' = \partial/\partial x$.

The kinetic energy T is given by

$$T = \underbrace{\frac{1}{2}\int_0^L m\left(\dot{w}^2 + \dot{v}^2 + \frac{I_o}{A}\dot{\phi}^2\right) \mathrm{d}x}_{T_B} + \underbrace{\frac{1}{2}\int_0^L m_t\left(\dot{w}_t^2 + \dot{v}_t^2\right) \mathrm{d}x}_{T_\mathrm{t}} + \underbrace{\left[\frac{1}{2}M_\mathrm{tip}(\dot{w}^2 + \dot{v}^2)\right]_{x=L}}_{T_\mathrm{tip}}, \tag{3}$$

where T_B is the kinetic energy of the beam, T_t is the kinetic energy of the tendon, T_tip is the kinetic energy associated with the tip mass, m is the mass per meter of the beam, m_t is the mass per meter of the tendon, M_tip is the mass of the attachment fixture that is used to attach the tendon, L is the length of the system, and $\dot{()} = \partial/\partial t$.

The virtual work δW of the non-conservative forces and moments acting on the beam is given by

$$\delta W = \int_0^L \left(F_w \delta w + F_v \delta v + Q_\phi \delta\phi\right) \mathrm{d}x, \tag{4}$$

where F_v and F_w are the excitation force in the y and z directions, and Q_ϕ is the moment about x axis. There are no external excitation forces applied to the tendon. The tendon motion is, however, excited through the coupling with the beam, which is realised through the tip plate. As it is assumed that the damping is very weak, so that it has negligible effect on natural frequencies and mode shapes, no virtual work of dissipative forces was included in Eq. (4).

Submitting Eqs. (2), (3) and (4) into Eq. (1), integrating by parts and separating the variables yields the following equations of motions

$$(EI_z w'')'' + (Pw')' + m\ddot{w} - F_w = 0, \tag{5a}$$

$$(EI_y v'')'' + (Pv')' + m\ddot{v} - F_v = 0, \tag{5b}$$

$$-(GJ\phi')' + (P\frac{I_o}{A}\phi')' + m\frac{I_o}{A}\ddot{\phi} - Q_\phi = 0, \tag{5c}$$

$$-(Pw_t')' + m_\mathrm{t}\ddot{w}_\mathrm{t} = 0, \tag{5d}$$

$$-(Pv_t')' + m_\mathrm{t}\ddot{v}_\mathrm{t} = 0, \tag{5e}$$

and the boundary conditions

$$\delta w\left\{[-(EI_z w'')' - Pw']|_0^L + M_\mathrm{tip}\ddot{w}|_{x=L}\right\} = 0, \tag{6a}$$

$$\delta w'\left\{EI_z w''|_0^L\right\} = 0, \tag{6b}$$

$$\delta v\left\{[-(EI_y v'')' - Pv']|_0^L + M_\mathrm{tip}\ddot{v}|_{x=L}\right\} = 0, \tag{6c}$$

$$\delta v' \left\{ EI_y v''|_0^L \right\} = 0, \tag{6d}$$

$$\delta\phi \left\{ [GJ\phi' - P\frac{I_o}{A}\phi'] \Big|_0^L \right\} = 0, \tag{6e}$$

$$\delta w_t \left\{ \ Pw_t'|_0^L \right\} = 0, \tag{6f}$$

$$\delta v_t \left\{ Pv_t'|_0^L \right\} = 0. \tag{6g}$$

In order to determine the boundary conditions at the free and fixed end, the usual logic is used [1], i.e. the displacements and slopes are zero at the fixed end, and their variations are arbitrary at the free end and hence their coefficients must be equal to zero individually. The former leads to the well known conditions for the fixed end, i.e. for $x = 0$

$$w = w' = v = v' = \phi = w_t = v_t = 0, \tag{7}$$

while the latter requires the expressions in curved brackets in Eq. (6) to be equal to zero, i.e. for $x = L$ the boundary conditions in which the coupling between the tendon and the beam has not been enforced can be written as

$$-(EI_z w'')' - Pw' + M_{\text{tip}}\ddot{w} = 0, \tag{8a}$$

$$EI_z w'' = 0, \tag{8b}$$

$$-(EI_y v'')' - Pv' + M_{\text{tip}}\ddot{v} = 0, \tag{8c}$$

$$EI_y v'' = 0, \tag{8d}$$

$$GJ\phi' - P\frac{I_o}{A}\phi' = 0, \tag{8e}$$

$$Pw_t' = 0, \tag{8f}$$

$$Pv_t' = 0. \tag{8g}$$

Equations (8a) and (8c) describe the shear effects at the tip of the beam. Equations (8b), (8d) and (8e) express the fact that there are no bending moments or torque applied at the tip, and Eqs. (8f) and (8g) describe the transversal forces at the end of the tendon.

In these boundary conditions, however, the important coupling between the tendon and the beam that is realised through the tip attachment fixture and through which the tendon is excited has not been taken into account. In order to introduce this coupling, suitable geometric and load continuity conditions are needed. The geometric coupling requires the equality of displacements of the beam and the tendon at the free end, i.e.

$$w_t(t, L) = w(t, L), \tag{9a}$$

$$v_t(t, L) = v(t, L). \tag{9b}$$

The load equilibrium is enforced by combining the boundary conditions in Eqs. (8f) and (8g), which can be interpreted as the shear forces acting on the tip plate, with the shear conditions in Eqs. (8a) and (8c). The shear equilibrium conditions (8a) and (8c) therefore become

$$-(EI_z w'')' - Pw' + M_{\text{tip}}\ddot{w} + Pw_t' = 0, \tag{10a}$$

$$-(EI_y v'')' - Pv' + M_{\text{tip}}\ddot{v} + Pv_t' = 0. \tag{10b}$$

In order to obtain the final set of boundary conditions, Eqs. (8f) and (8g) are replaced by Eqs. (9a) and (9b), leading to the set of BCs given by Eqs. (8b), (8d), (8e), (9) and (10). The final set of BCs is summarised and further discussed in section 2.2.

2.2. Final equations of motions and boundary conditions

The final equation of motion describing the cantilever beam with uniform parameters loaded by the tendon are

$$EI_z w'''' + Pw'' + m\ddot{w} = F_w, \tag{11a}$$

$$EI_y v'''' + Pv'' + m\ddot{v} = F_v, \tag{11b}$$

$$-GJ\phi'' + P\frac{I_o}{A}\phi'' + m\frac{I_o}{A}\ddot{\phi} = Q_\phi, \tag{11c}$$

$$-Pw_t'' + m_t\ddot{w}_t = 0, \tag{11d}$$

$$-Pv_t'' + m_t\ddot{v}_t = 0. \tag{11e}$$

The boundary conditions for the fixed end ($x = 0$) are

$$w = w' = v = v' = \phi = w_t = v_t = 0 \tag{12}$$

and for the free end ($x = L$) are

$$-EI_z w''' - Pw' + M_{\text{tip}}\ddot{w} + Pw_t' = 0, \tag{13a}$$

$$EI_z w'' = 0, \tag{13b}$$

$$-EI_y v''' - Pv' + M_{\text{tip}}\ddot{v} + Pv_t' = 0, \tag{13c}$$

$$EI_y v'' = 0, \tag{13d}$$

$$GJ\phi' - P\frac{I_o}{A}\phi' = 0, \tag{13e}$$

$$w_t = w, \tag{13f}$$

$$v_t = v. \tag{13g}$$

Equations (11)-(13) create a system of two forth-order and three second-order partial differential equations (PDEs) with the corresponding number of boundary conditions. Since there is no coupling between the different motions of the beam, and the coupling between the beam and the tendon is realised through the tip mass only, there are no coupling terms in the equation of motion in Eq. (11). Therefore, Eqs. (11a), (11b) and (11c) are formally the same as the PDEs for the bending and torsion of an axially loaded beam [1, 8, 9] and Eqs. (11d) and (11e) formally appear to be the well-known wave equations [4, 7]. However, the crucial difference between the developed system and the well-known equations lie in the boundary conditions that ensure the coupling between the beam and the tendon. In particular, Eqs. (13a) and (13c) prescribe the force equilibrium at the tip, and Eqs. (13f) and (13g) enforce the same tip displacements of the beam and the tendon. Due to these coupling conditions, the motion of the beam excites the tendon which influences the beam by applying the axial force. It can be therefore expected that there will be an interaction between the bending of the beam and transversal motion of the tendon (the y and z direction are, however, uncoupled due to symmetric cross-section and isotropic material). As can be seen in Eq. (13e) there is no coupling in the torsional boundary condition since the tendon coincides with the neutral axis about which the cross-section rotates. This implies that although the torsional modes are influenced by the tendon-induced axial force, they do not interact directly with the tendon.

2.3. Numerical modal analysis

In order to evaluate the modal properties (natural frequencies and mode shapes) of the beam-tendon system, the excitation forces and moments in Eq. (11) are set to zero and an assumption of the normal mode is used. A solution of any given dependent variable is expressed as the multiplication of the time-invariant mode shape and the time-varying harmonic function of the constant frequency in the following form

$$\begin{gathered} w(t,x) = W(x)\mathrm{e}^{\mathrm{i}\omega t}, \quad v(t,x) = V(x)\mathrm{e}^{\mathrm{i}\omega t}, \quad \phi(t,x) = \Phi(x)\mathrm{e}^{\mathrm{i}\omega t}, \\ w_{\mathrm{t}}(t,x) = W_{\mathrm{t}}(x)\mathrm{e}^{\mathrm{i}\omega t}, \quad v_{\mathrm{t}}(t,x) = V_{\mathrm{t}}(x)\mathrm{e}^{\mathrm{i}\omega t}, \end{gathered} \tag{14}$$

where ω is the angular natural frequency, and $W(x), V(x), \Phi(x), W_t(x), V_t(x)$ are the components of the mode shape which represent, respectively, the bending in the z and y directions, the rotation about the x axis, and the transversal motion of the tendon in the z and y directions. The complete mode shape of the system can then be formally written as $\Psi(x) = [W(x), V(x), \Phi(x), W_t(x), V_t(x)]$. The mode shape is normalised so that the value of the dominant component is equal to unity at the tip. Since there is no bending-torsion coupling, some of the components are zero for a given natural frequency. For example, the beam-tendon system vibrating in the z direction has non-zero only $W(x)$ and $W_t(x)$ components since the other components are not excited. For the clarity of presentation, only non-zero components will be displayed in the results. In addition, the following terminology will be used in the rest of the paper. If the mode shape is given by the motion of the beam, it will be refer to as a beam-dominated mode. On the other hand, if the mode shape is determined by the tendon, the term tendon-dominated mode will be used instead.

Substituting the normal mode forms into Eqs. (11), (12) and (13) allows one to eliminate time and rewrite the PDEs into a system of first order ordinary differential equations (ODEs) that, together with the BCs, define a boundary value problem. This boundary value problem is then be solved by a Matlab bvp4c solver [21] for the unknown natural frequencies ω and corresponding mode shape components $W(x)$, $V(x)$, $\phi(x)$, $W_{\mathrm{t}}(x)$ and $V_{\mathrm{t}}(x)$. This solver is very versatile since it uses a collocation method but may suffer from a decreased numerical performance if an appropriate starting guess is not provided.

In order to obtain an appropriate starting guess, the following process, which is similar to the one used in [20], was implemented. Instead of removing the excitation forces and moments in Eq. (11), the harmonic excitation is assumed. By submitting the normal mode assumption to the system of equations with the harmonic forcing, a slightly different boundary value problem can be defined. In this boundary value problem, the excitation frequency ω is known and the response $W(x)$, $V(x)$, $\phi(x)$, $W_{\mathrm{t}}(x)$ and $V_{\mathrm{t}}(x)$ can be evaluated from any non-zero starting guess easily. The natural frequencies and the mode shapes can then be approximately estimated from the obtained responses and used as the initial guesses to evaluate the natural frequencies and mode shapes accurately.

3. Experimental validation

In this section, the theoretical model is validated using a bench-top experiment. Firstly, the experimental set-up is described, then the updating of the underlying beam model is carried out so the full beam-tendon system can be eventually validated for multiple tendons and a range of loading conditions.

3.1. Experimental set-up description

The picture of the bench-top experiment can be seen in Fig. 2. The beam with a box cross-section is rigidly clamped at one end and free at the other end. The tendon is attached to the tip using a small rigid plate mounted at the free end of the beam, and passes freely inside the beam towards the clamp where its traversal motion is mechanically constrained using a small magnet. The magnet is attached to the tendon and attracted by the steel clamp. It ensures that the tendon is centred in the geometric centre of the beam's cross-section and can slide in the axial direction as necessary. This constrain also allows the tendon to be modelled as having the same length as the beam. The tendon then continues through the clamp and pulley and is attached to a hanging platform. The tension of the tendon, and hence the axial load applied to the beam, is controlled by the amount of weight placed on the platform.

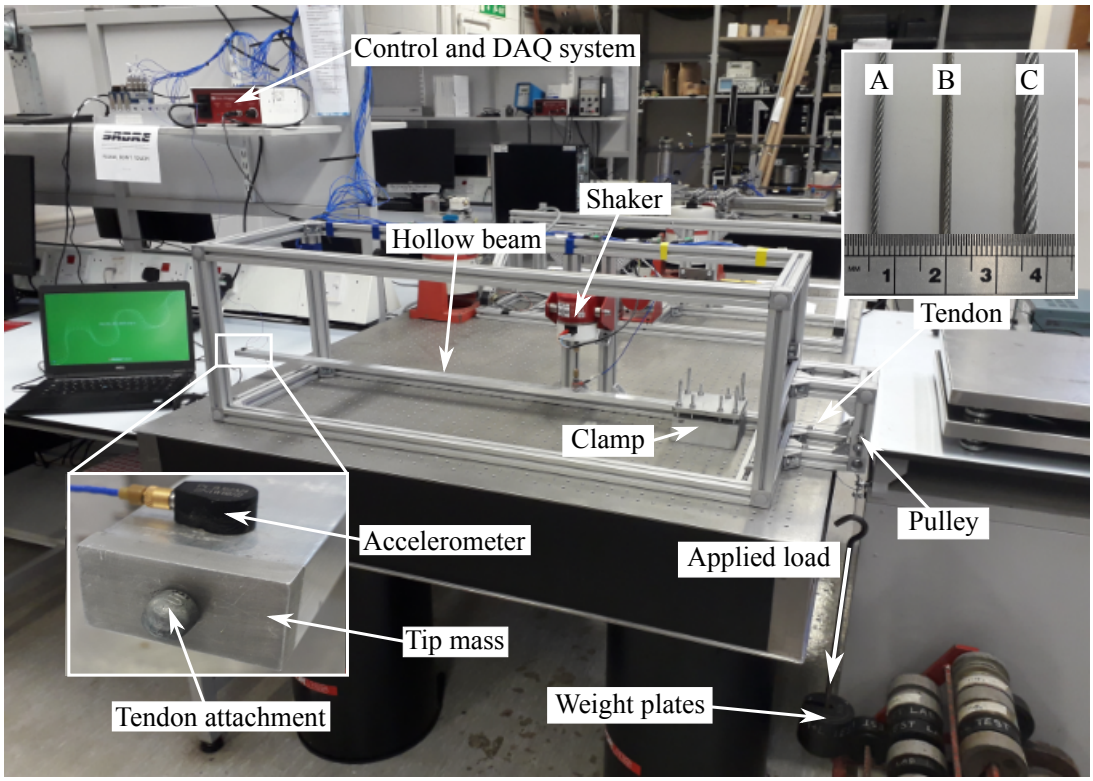

Figure 2: Experimental set-up. The cantilever beam subjected to the tendon-induced axial force generated by the applied load is excited by a shaker to obtain the frequency response functions for the estimation of modal properties which are then used to validate the theoretical model.

The computed nominal properties of the beam seen in Fig. 2 are $L = 1\,\mathrm{m}$, $A = 11.16 \times 10^{-5}\,\mathrm{m}^2$, $EI_z = 191.09\,\mathrm{N\,m}^2$, $EI_y = 603.35\,\mathrm{N\,m}^2$, $GJ = 175.86\,\mathrm{N\,m}^2$ and $I_o = 11.43 \times 10^{-9}\,\mathrm{m}^4$. The beam was weighed and the distributed mass was found to be $m = 0.2929\,\mathrm{kg\,m}^{-1}$. Several tendons were used in this study as seen in the inset in Fig. 2. For the majority of presented results, the middle-size tendon B, with $m_t = 0.0125\,\mathrm{kg\,m}^{-1}$ is used. Tendons A and C are then used in section 3.5 to study the effect of the tendon mass. Their mass per meter is $0.008\,\mathrm{kg\,m}^{-1}$ and $0.0285\,\mathrm{kg\,m}^{-1}$, respectively. The mass of the tip plate is 0.0052 kg and the tendon attachment weighs approximately 0.001 kg so the total tip mass was $M_{\mathrm{tip}} = 0.0062\,\mathrm{kg}$.

The beam is excited using a modal shaker to obtain frequency response functions (FRFs). The shaker was controlled via a modular control and data acquisition (DAQ) system. Random excitation was used to excite the frequency range between 5 and 450 Hz and the response data were recorded using a small uni-directional accelerometer. The weight of the used accelerometer was less than 1 g so it was not included in the theoretical model. A higher number of accelerometers was not used because it was found that their combined mass had a significant disturbing influence on the modal properties of the system and prevented good comparison with the computed results. For the measurement of the frequency-loading (F-L) diagrams, which depict the natural frequencies as a function of the applied load, the accelerometer was placed at the tip of the beam as seen in Fig. 2. The accelerometer was moved along the x axis to measure the mode shapes when required. The load was varied using the weights placed on the hanging platform in two kilogram increments from 2 kg to 50 kg. The response data and the input force were used to estimate the FRFs using the H_v-estimator [22] and the natural frequencies, damping and mode shapes were estimated using the least-square complex frequency (LSCF) estimator [23]. The measurement was performed firstly in the z direction and then in the y direction by rotating the beam in the clamp by 90 degrees (the shaker remained vertical).

Each individual measurement was repeated three times to evaluate the repeatability of the experimental results and to eliminate potential errors in the measurement chain and signal processing. The average of the estimated modal properties is always shown in the following results and, when appropriate, the standard deviation is added as well.

3.2. Underlying beam model validation

Before including the tendon into the experiment, the model of the beam with and without the tip mass was validated. The purpose of this step was to obtain the underlying model of the beam, which is defined using the PDEs in Eqs. (11a)-(11c) with $P = 0$, as accurately as possible so that the effect of the tendon can be studied separately.

Firstly, the beam without the tip mass is considered. The comparison of the experimental and computed natural frequencies is given in Tab. 1 and visualised in Fig. 3. In total, seven bending modes were

	f^{exp} [Hz]	std [Hz]	ζ [%]	std [%]	f^{nom} [Hz]	error [%]	f^{upd} [Hz]	error [%]
1W	13.27	0.0017	0.485	0.0092	14.29	7.70	13.01	-1.99
1V	24.50	0.0010	0.065	0.0063	25.40	3.68	23.52	-4.01
2W	81.59	0.0032	0.491	0.0123	89.59	9.80	81.51	-0.09
2V	147.40	0.0013	0.023	0.0061	159.18	7.99	147.40	0.00
3W	219.33	0.0587	0.369	0.0984	250.84	14.37	228.23	4.06
3V	389.00	0.0451	0.027	0.0051	445.72	14.58	412.72	6.10
4W	421.15	0.0462	0.226	0.0057	491.55	16.72	447.24	6.19

Table 1: Comparison of experimental and computed natural frequencies and their relative errors for the beam without the tip mass. xV and xW stands for the x^{th} bending mode in the y and z direction, respectively, f^{exp} are experimentally measured natural frequencies, ζ are the damping ratios, f^{nom} are the computed natural frequencies using the nominal parameters and f^{upd} are the computed natural frequencies using the updated parameters

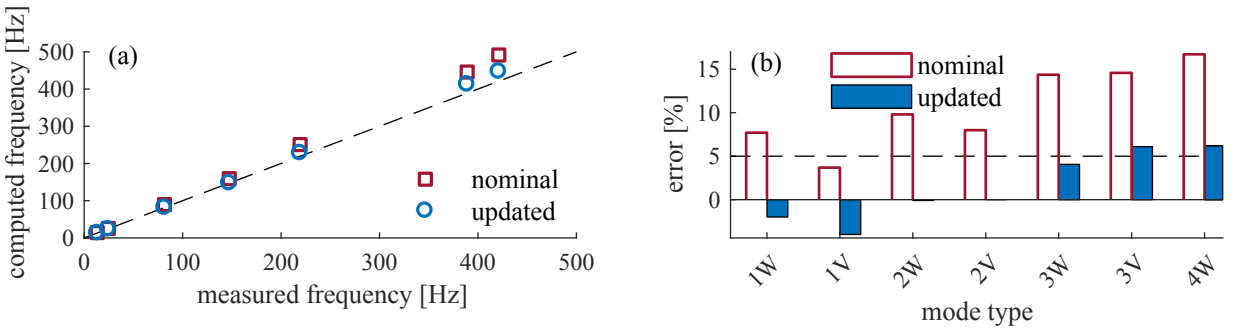

Figure 3: Comparison of the experimental and computed natural frequencies without the tendon and no tip mass: (a) the average values and (b) the relative error. The standard deviation of experimental frequencies is smaller than the size of the markers so it is not shown.

measured in the considered frequency range. Four of these modes represent the bending in the z direction (marked by xW) and remaining three represent the bending in the y direction (marked by xV). The standard deviation of the measured natural frequencies is very small, not exceeding 0.06 Hz, which indicates a very good repeatability of the measurement and accuracy of the used modal parameter estimation method. The damping ratio ζ was also measured despite not being used in the model. It can be seen that the damping ratios as well as their standard deviations are very low (less than 0.5 % for all modes) so it can be assumed that the damping has negligible effect on the natural frequencies and so the theoretical model used is valid even without the dissipative effects.

The natural frequencies computed using the nominal parameters (marked by f^{nom}) are compared to the experimental values (marked by f^{exp}) in Tab. 1 and Fig. 3. It can be seen that the error of the

computed frequencies is quite significant since the relative error of almost all modes is greater than 5 % with the greatest error almost 17 %. Therefore, it was decided to update the model parameters such that the difference between the measured and computed modal properties is minimised. The bending rigidities EI_y, EI_z were updated since the mass of the beam was measured and no other parameters influence the bending natural frequencies. The updating was performed using a single-objective multi-variable optimisation using a genetic algorithm [24], whereby the objective function was defined by the error between the measured and computed natural frequencies. Mathematically, this problem can be written as

$$EI_y^{\mathrm{upd}}, EI_z^{\mathrm{upd}} = \underset{EI_y, EI_z}{\operatorname{argmin}} \frac{1}{N_m} \sum_{i=1}^{N_m} \left| 1 - \frac{f_i^{\mathrm{exp}}}{f_i^{\mathrm{com}}(EI_y, EI_z)} \right|, \tag{15}$$

where $N_{\mathrm{m}} = 7$ is the number of the natural frequencies taken into account. The mode shapes have not been included in the objective function, because all the modal assurance criteria (MAC) [25] values were very close to 1 even without updating.

The updated bending rigidities, EI_y^{upd}, EI_z^{upd} were 517.33 N m^2 and 157.79 N m^2, respectively, which represents 85.7 % and 82.6 % of their nominal values, respectively. The updated natural frequencies (marked by f^{upd}) and their comparison with the experimental values can be seen in Tab. 1 and Fig. 3. The overall character of the error between the measured and updated frequencies is very different. The error of almost all modes has decreased under the 5 % threshold. The error of the 6$^{\mathrm{th}}$ and 7$^{\mathrm{th}}$ mode, despite decreasing significantly, remained higher than 5 %.

Having identified the parameters of the beam model without the tip mass, the tip mass was added, and the resulting computed (marked by f^{com}) and corresponding experimental results are compared in Tab. 2 and Fig. 4. No additional updating was performed because the tip mass could be easily measured. As expected,

	f^{exp} [Hz]	std [Hz]	ζ [%]	std [%]	f^{com} [Hz]	error [%]
1W	12.77	0.0013	0.496	0.0327	12.56	-1.60
1V	23.61	0.0017	0.074	0.0021	22.72	-3.76
2W	79.05	0.0037	0.456	0.0378	78.90	-0.19
2V	142.94	0.0117	0.029	0.0058	142.68	-0.18
3W	212.83	0.0171	0.408	0.0672	221.29	3.97
3V	378.27	0.0234	0.031	0.0049	400.17	5.79
4W	408.97	0.0062	0.171	0.0046	434.30	6.19

Table 2: Comparison of the experimental and computed natural frequencies and their relative errors for the beam with the tip mass

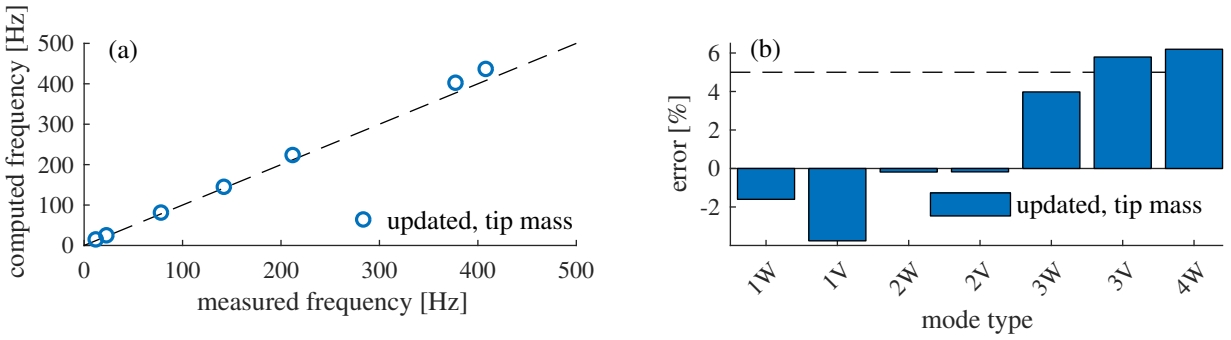

Figure 4: Comparison of experimental and computed natural frequency with the tip mass and no tendon: (a) average values and (b) the relative error.

the magnitude of all measured natural frequencies reduced when the tip mass was added, while the standard

deviation did not significantly changed. The damping ratios have not been significantly influenced by the presence of the tip mass. As seen from the comparison of computed and experimental natural frequencies, the errors have decreased when the tip mass was added. The error of the 6^{th} and 7^{th} mode is still higher than 5 %. The errors of all other modes are lower than 5 % which is herein considered as an acceptable error. It is believed that the remaining error at higher modes is caused by an inherent feature of Euler-Bernoulli theory that is known to overestimate the natural frequencies of higher modes [6, 26].

Up to this point, mainly the natural frequencies have been discussed. However, the modes shapes were also extracted from the measured FRFs. The comparison the mode shapes computed using the updated rigidities and including the tip mass with the experimentally measured ones is shown in Fig. 5. As can

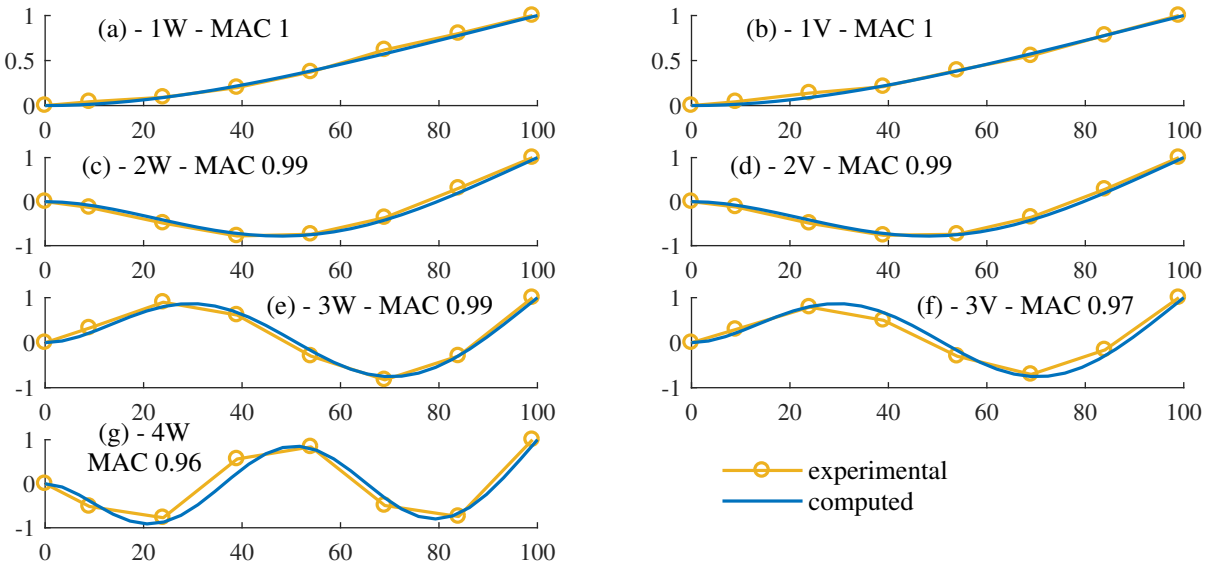

Figure 5: Comparison of the measured and computed beam mode shapes components ($W(x)$ and $V(x)$), and their auto MAC values: (a)-(g) the first seven bending modes shapes (the x-axis is the position along the beam in centimetres while the y-axis shows the values of the mode shapes). The components of the mode shapes that are not shown are equal to zero.

be seen all the MAC values are higher than 0.96 so the agreement between the experimentally measured and computed modes shape is very good. When compared with the predicted mode shapes, the measured mode shapes indicate slightly increased mobility in the proximity of the fixed root boundary condition. It is therefore possible that further modelling improvement can be achieved by introducing more detailed root boundary condition. However, this effort is not followed further here because the developed model is deemed to be sufficiently representative of the under-lying beam dynamics.

3.3. The beam-tendon model validation

In the previous section, the parameters of the beam model have been updated using the experimental data obtained for the beam without the tip mass and it was shown that the error of this model remained acceptable even when the tip mass was added. In this section, the validation of the full systems of PDEs (Eq. (11)) and BCs (Eq. (12) and (13)) describing the beam-tendon system is performed. The validation is performed for the middle-size tendon B (seen in Fig. 2). In the following, the applied load is discussed in terms of weight placed on the hanging platform, marked as M_{L}, since this is intuitively easier to interpret. The relation between the tendon tension and the weight is approximately $P = M_{\text{L}}g$, where g is a gravitational constant equal to 9.81 $\text{m}\,\text{s}^{-2}$ and the effect of the friction between the tendon and the pulley is assumed to be negligible.

The frequency-loading diagram obtained for the y and z directions is shown in Fig. 6. The average of the experimentally measured natural frequencies is shown using the markers (the standard deviation is smaller

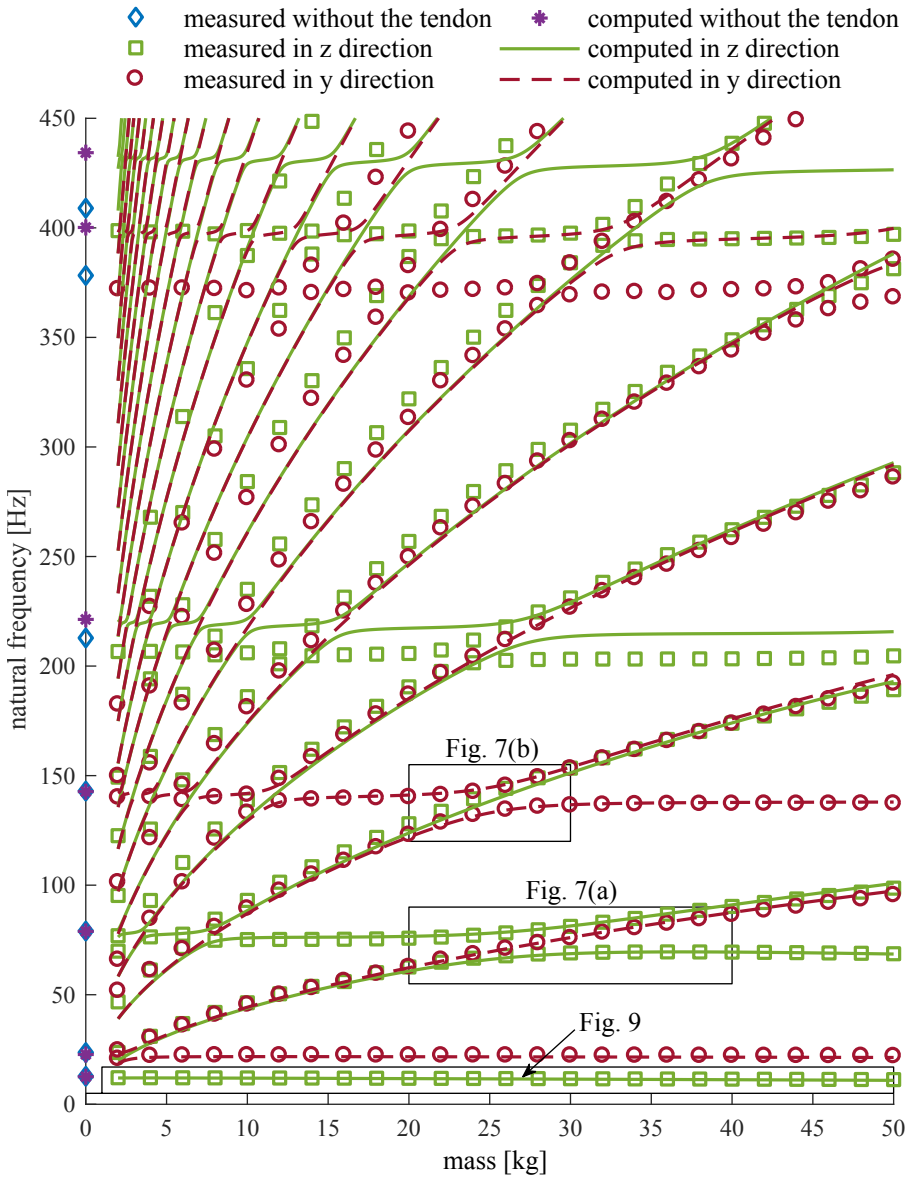

Figure 6: The frequency-loading (F-L) diagram showing the dependence of the natural frequencies on the applied load for the middle-size tendon B.

than the size of the markers, so it is not shown for clarity), and the computed results are shown using solid and dashed lines. The measured and computed natural frequencies of the beam with the tip mass but no tendon (from Tab. 2), are also shown as a reference.

Two sets of frequency loci can be distinguished in the F-L diagram. There are seven beam-dominated modes present whose frequency loci appear to be almost parallel to the x-axis, but in fact, they decrease slightly with the increasing load. This decrease in the natural frequencies is caused by the tendon-induced axial force which increases by increasing the applied force. The same effect of the compressive axial force was also observed in studies about structural stability of axially-loaded beams [8, 9]. This decrease is emphasised in more detail for the first mode in Fig. 9. It can also be noticed that for very low applied load, these frequency loci are very close to the natural frequencies obtained for the beam without the tendon.

The other set of natural frequencies, which increase rapidly with the added weight, are the tendon-dominated modes. Experimentally, eight of such modes were captured, while numerically many more were computed in the low applied weight region (approximately $< 5\,\mathrm{kg}$) where it was not possible to excite these modes experimentally. It can be noticed in the upper part of the F-L diagram that there is a small difference in the frequencies of tendon-dominated modes measured in the y and z directions. The former set of frequencies are lower than the latter ones. However, the values of the natural frequencies of the tendon-dominated modes are expected to be the same in both directions (as also confirmed by the numerical results) since the tendon is symmetric. The error in the experimental measurements is probably related to the change of the test-rig layout that must have been made to measure the system vibration in the y direction. The orientation of the beam-tendon system was changed by rotating it by 90 degrees such that the y direction could have been measured while keeping the shaker in its original vertical position. This change also required the adjustment of the transversal tendon attachment in the clamp realised by a magnet. This change of the layout then probably yielded the discrepancies between the two sets of the tendon-dominated modes. However, as seen in the F-L diagram in Fig. 6, they are not significant at lower modes and manifest themselves only at higher ones, so they do not jeopardise the validity of the results.

The beam-dominated and tendon-dominated modes interact with each other through the frequency loci veering phenomenon [17, 27, 28]. The number of veering interactions is very high for the higher frequency and lower loading region due to the presence of the large number of the tendon-dominated modes. Two selected veering regions, including the measured beam mode shape components and damping ratios, are discussed in more detail in section 3.4. It is noted that when not veering the tendon-dominated modes are characterised by very low beam activity. Consequently, this aspect of the tendon dynamics asymmetry is found to be negligible when away from the veering regions. On the other hand, in this study, an approach to the veering regions is accompanied by increasing beam activity in one bending direction. This is the stage when the boundary condition asymmetry produces selective modal interaction between the two initially nearly identical tendon frequencies, with one mode featuring veering and the other continuing unaffected toward modal crossing.

Overall, the agreement between the experiment and theoretical results is very satisfactory. In particular, the bottom half of the F-L diagram exhibits an excellent agreement. In the upper half, the computed and experimentally measured modes show the same trends, but with the systematic errors manifested as the frequency offsets. It can be noticed, especially in the last three beam-dominated modes, that the frequency offset is almost constant for all applied weights. Moreover, this offset is equal to the initial error between the measured and computed values for the beam with the tip mass, but without the tendon. Therefore, it can be concluded that since the error between the measured and experimental frequency loci at higher frequencies is invariant to the applied load while the correct anticipated trends are observed, the effect of the tendon is captured correctly by the theoretical model and the discrepancies merely originate from the error given by the underlying beam model.

3.4. Veering in the beam-tendon system

The veering phenomenon, whereby two frequency loci veer away and diverge instead of crossing, has been observed in many structural systems [17, 27]. During veering, the modes swap all their properties and the mode shapes rapidly rotate [28]. The veering typically occurs due to a variable parameter whose increase leads to smooth changes in the natural frequencies and hence their interaction. In the beam-tendon system, the veering is caused by the variation of the tendon-induced axial force.

Two of the many veering regions seen in Fig. 6 are enlarged in Fig. 7. The natural frequencies are displayed including their standard deviations. The computed and experimentally measured mode shape components of the beam ($W(x)$ and $V(x)$) and estimated damping ratios are also added to illustrate the veering. Since it was not possible to place any sensor on the tendon, its mode shape contributions ($W_\mathrm{t}(x)$ and $V_\mathrm{t}(x)$) could not have been experimentally measured so only the computed results are shown.

There is a major difference between Fig. 7(a) and Fig. 7(b). While the former shows the veering between the bending and tendon modes in the z direction, the latter shows the veering between the modes in the y direction. In both cases, the tendon-dominated mode in the orthogonal direction passes through the veering region unchanged. Before and after the veering region, the tendon-dominated modes in both directions are

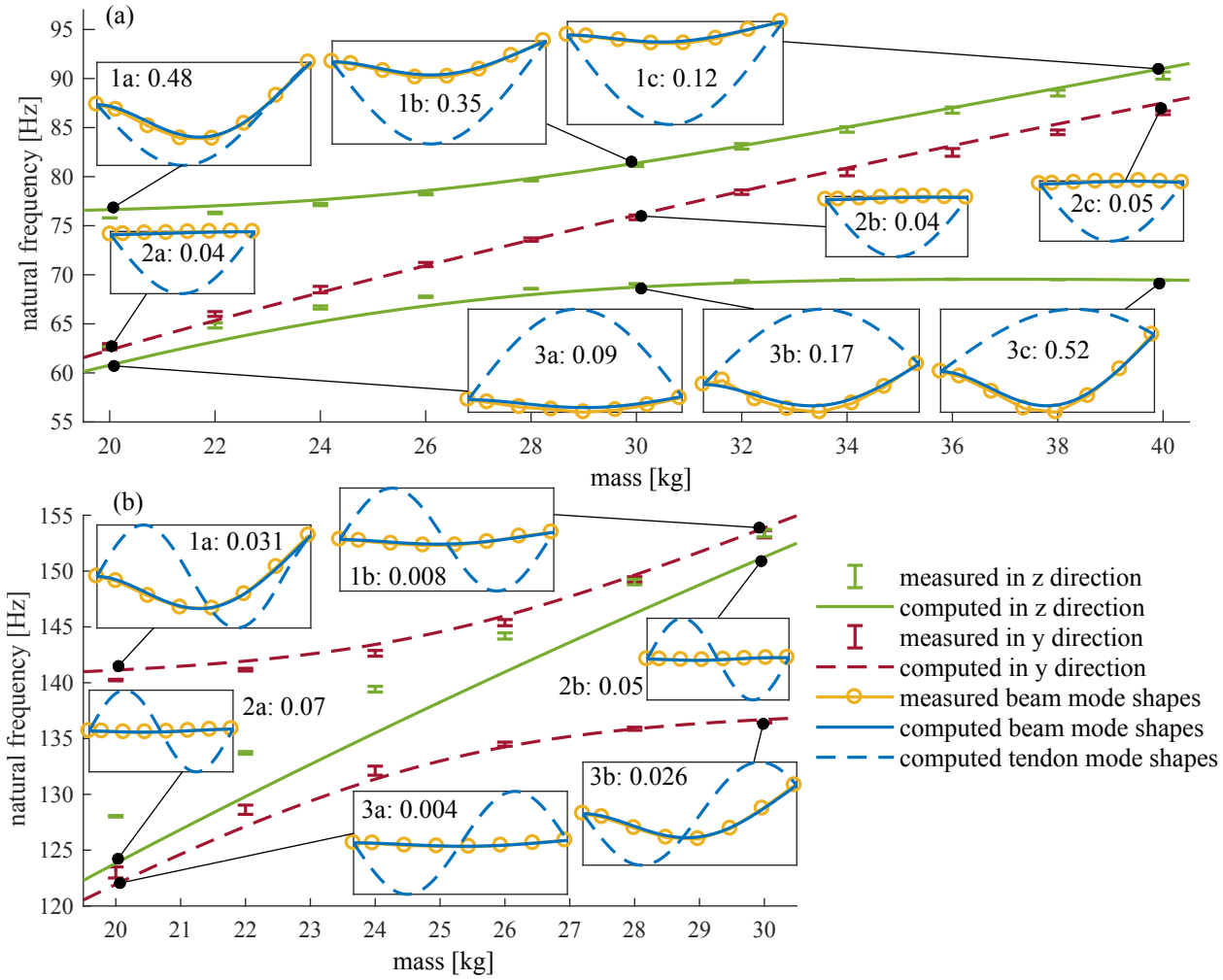

Figure 7: Frequency loci veering in the beam-tendon system: (a) in the z direction and (b) in the y direction. The numerical values in the insets are the experimentally estimated damping ratios ζ in %.

identical due to the cross-sectional symmetry of the tendon as seen in Fig. 6. However, when approaching the frequency locus of the beam-dominated mode, the tendon-dominated mode in the corresponding direction starts to veer away from the beam-dominated mode while the other tendon-dominated mode (which has the same shape, but in the orthogonal direction) continues through the veering region unchanged.

Both veering regions exhibit the typical signs of veering - with the increasing tendon tension, two frequency loci initially converge, but then suddenly diverge and follow the trajectory of the other mode while swapping all their properties including the damping ratios and mode shapes that also changes phase. For example, focusing on Fig. 7(a) it can be seen that the beam component of the mode shape in inset 1a is the same as the corresponding mode shape component in inset 3c which is associated with the different frequency locus and where the orientation of the tendon mode shape component changed. Similarly, the mode in inset 3a swapped with that in 1c and the orientation of the tendon mode shape component changed. As explained, the frequency curve which passes through the veering regions unaffected is associated with the motion of the tendon in the orthogonal bending direction. Since it is not influenced by the veering the associated mode shapes and damping ratios are unaffected. The agreement between the experimentally measured and computed modes shapes is very good since virtually no discrepancies can be observed.

The extracted damping ratios also seem to demonstrate all signs of veering. Although the damping ratios

were measured with the standard deviations higher than the ones for the beam without the tendon, it is apparent that the tendon-dominated modes are lightly damped (with the damping ratio about 0.1 %) while the damping ratio of the beam-dominated modes is higher (about 0.5 % for the bending in z direction). Additionally, the damping ratios measured for the beam-dominated modes of the beam-tendon system are very close to those measured for the beam without the tendon as documented in section 3.2. This indicates that the tendon does not introduce any substantial damping effects into the system. All the observations presented for Fig. 7(a) can be equally made for Fig. 7(b), including the mode shape and damping ratio swaps.

3.5. Effect of the tendon mass

So far, only the tendon B (seen in Fig. 2) has been used. In this section, two more tendon sizes, one thinner and one thicker than the tendon B, are tested. Besides the difference in the tendon, the test rig and measurement procedure were exactly the same as in the previous cases. The measurements were performed in the z direction only.

The comparison of the measured and computed F-L diagrams is shown in Fig. 8. It can be seen that

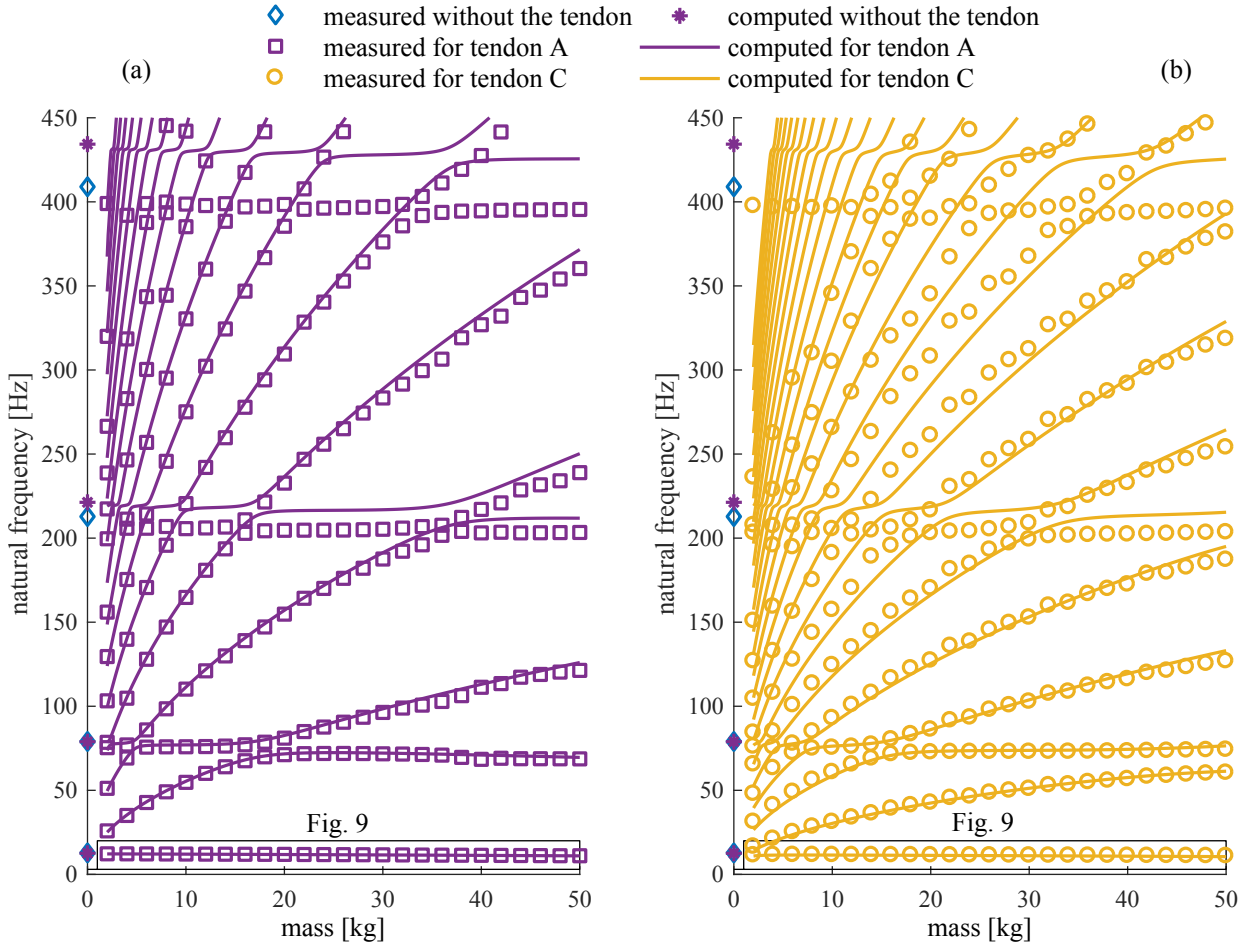

Figure 8: Frequency-loading diagrams for the beam-tendon system: (a) thin tendon A and (b) thick tendon C. The number of tendon-dominated modes and their rates of increase are different in each case.

the agreement between the two sets of results is very good. The discrepancies can be explained by the same argumentation as in section 3.3 for the tendon B, i.e. the frequency offsets occurring in the upper half of the F-L diagram for the beam-dominated modes are caused by the error in the underlying beam model.

The effect of the tendon mass is apparent when comparing Fig. 8(a), Fig. 6 and Fig. 8(b), which were obtained for the thin, medium, and thick tendon, respectively. The natural frequencies of the tendon-dominated modes for the thicker tendons are lower than those for the thinner ones and their rate of frequency increase with the load is also more gradual. This means that heavier tendons produce the F-L diagram that is more densely populated by the tendon-dominated modes than the same F-L diagram obtained for the lighter tendons. Consequently, the veering regions shift so they appear at lower loading. For example, the veering region studied in Fig. 7(a) that occurred in a proximity of 30 kg for tendon B, shifted to 18 kg for the thin tendon A and is not visible at all for the tendon C (the veering presumably takes place around 60 kg which is outside the measured loading range). Similar shifts can be observed for all other veering regions as well.

The good global agreement between the computed and experimental results has been obtained for all presented results. Here, the focus is on the fine agreement between the measured and computed frequency loci of the first mode. The first bending mode (1W) for all three tendons is shown in Fig. 9. The standard

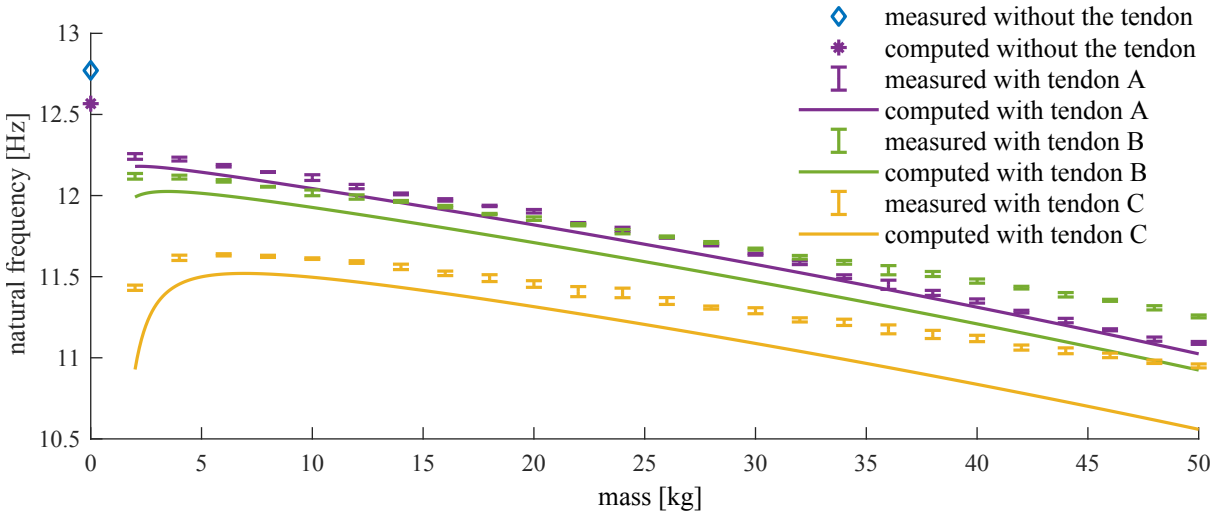

Figure 9: Comparison of the experimental (shown including the standard deviation) and computed natural frequencies of the first bending mode for the beam-tendon system with all three tested tendons.

deviation displayed is very small - in a vast majority of cases it is much less than 0.1 Hz which gives confidence in the experimental repeatability. The computed frequencies are slightly lower than the measured ones even for the very low loading. As in the previous cases, this is consistent with the error that originates from the underlying model of the beam. It is seen that thicker the tendon, lower the frequency for given load. This is in line with the increase of the total mass of the system caused by the presence of the heavier tendon. All the experimental and computed frequency loci decrease with increasing load. However, their rates of decrease are different. For the computed frequency loci, the rates of decrease seem to be the same while for the experimental results, slight differences can be observed between the used tendons. These differences can be explained by the presence of the pulley in the experimental set-up that introduces some friction. For the thinnest and lightest tendon A, the rate of decrease matches well to the computed one. This is observed, because the contact area between the pulley and the tendon is minimal. For the middle-size tendon B, the rate of decrease of the experimental frequencies is slightly different from the measured one. It appears as if more applied load (weight placed on the hanging platform) would be needed to obtain the computed rate of decrease. This implies that the tendon-induced axial force at the tip of the beam is lowered, most likely, by the friction between the pulley and the tendon. This consequently causes the slight difference between the measured and computed results. The effect is further magnified for the thickest and heavies tendon C, which produced the most significant discrepancies with the increasing load, because there is a large contact area between the pulley and the tendon. Therefore, all the features observed in Fig. 9 can be satisfactory

explained. Moreover, the discrepancies due to friction are very small occurring in the range of tenths of a hertz.

4. Further numerical studies

In this section, two numerical studies that extend the results beyond the capacities of the experiment are presented. Firstly, the effect of the tendon on the torsional vibration mode is studied and secondly, the structural stability of the beam-tendon system is investigated. These studies are performed for the beam-tendon system which was previously validated using the experiment.

4.1. The effect of the tendon on torsional vibration modes

The effect of the tendon B on the first torsional vibration mode is studied. It can be seen from the governing PDEs (Eq. (11)) and the BCs (Eq. (12) and Eq. (13)) that the torsional modes are influenced only by the tendon-induced axial force P, but are not coupled with the motion of the tendon in any direction. Therefore, there should be no interaction between the torsional modes of the beam and tendon-dominated ones. This is also confirmed by the numerical results shown in Fig. 10. From the computational standpoint,

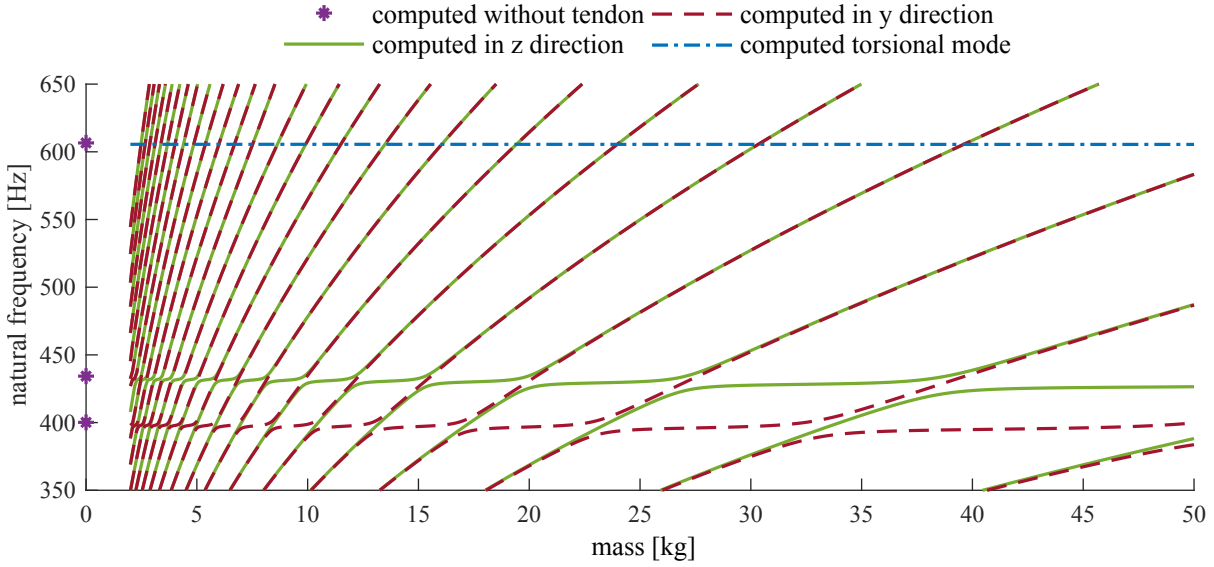

Figure 10: The effect of the tendon on the torsional modes. While the veering is present between tendon-dominated and bending modes of the system, no veering with the torsional mode is produced.

it is clear that the first torsional mode is not coupled with the rest of the modes because there is no veering observed across the locus of that mode. The distinction between the bending and torsional modes is very clear. While the higher bending modes interact with the tendon-dominated modes (many veering regions can be seen), the torsional mode is completely unaffected by the presence of the tendon-dominated modes as they cross the torsional mode. However, the tendon-induced axial force still causes a slight decrease of the natural frequency of the torsional mode (less than 0.05 Hz) in the considered loading region. It was suggested in [18] that if the tendon is placed eccentrically (away from the neutral axis) or, if there is bending-torsion coupling due to the offset between the elastic and mass axes of the beam, the tendon will have more pronounced effect on the torsional modes. However, a more detailed study and experimental demonstration of this phenomenon must be carried out in the future.

4.2. Structural stability

The final numerical study investigates the structural stability of the system. As the beam is axially loaded the structural stability may be of concern in a number of practical applications. The loss of structural stability occurs at the critical force when the lowest natural frequency of the system reaches zero [7–9]. In order to find the critical force, the F-L diagram is computed for a wider range of the tendon tension so the first two natural frequencies (1W and 1V) drop to zero. The F-L diagram for the first two modes is shown in Fig. 11. It can be seen that the natural frequencies do not decrease in a linear manner over the

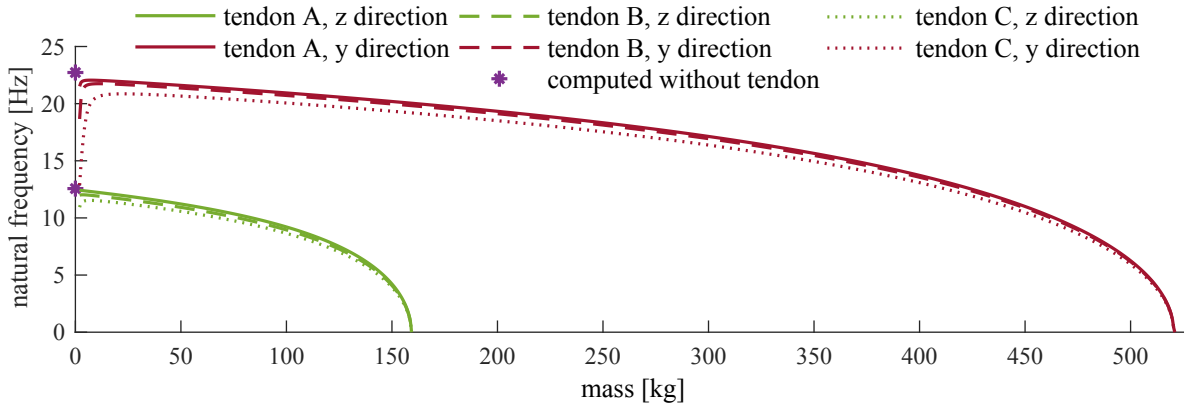

Figure 11: Structural stability of the beam-tendon system. The first two critical loads of the system are given by the weights in which the frequency loci intersect the x-axis.

whole loading region. For the low applied load, the frequency loci decrease gradually, but later the decrease becomes rapid in the close proximity of the critical load. This trend is in line with the studies of an axially loaded cantilever beam [7]. From Fig. 11, the computed critical loads are 158.78 kg and 520.45 kg. The critical force does not depend on the tendon mass as seen in Fig. 11. This is understandable, because the loss of stability occurs due to the applied axial load which is invariant to the tendon properties and its motion. The same critical loads can also be computed analytically for a model of buckling column loaded by an axial force that points to a fixed point. Such model was developed to represent a situation in which the axial force is induced by a cable [9]. Therefore, although the analytical theory only models the loading effect of the cable and the theoretical model developed in this paper models the motion of the cable, both models should yield comparable critical forces. The analytical expression for the first critical force obtained using the analytical model in [8, 9] reads

$$P_{\mathrm{cr}} = \frac{\pi^2 EI}{L^2}, \tag{16}$$

and the critical weight is equal to P_{cr}/g. Evaluating the analytical critical force for the z and y directions gives the value of 158.75 kg and 520.47 kg, respectively. Therefore, both models lead to the same critical force. This can be considered to be an additional validation of the developed model. As noted in [9] the obtained critical force is four times greater than the classical Euler bucking force of an axially loaded cantilever beam. This is caused by the emergence of the transverse forces at the tip of the beam, which are included in the boundary conditions in Eqs. (13a) and (13c) as the shear forces and which counteract the tendency for bucking and therefore lead to the higher critical load.

5. Discussion

In the previous sections the theoretical model of the coupled beam-tendon system has been derived, its experimental validation has been conducted and two further numerical studies have been presented. In this section, the main findings, assumptions and limitations, and a possible application of the beam-tendon system are discussed.

The validation of the theoretical model derived using Hamilton's principle was conducted using the bench-top experiment. Throughout the paper, a good agreement between the experimental and computed results has been shown and it has been found that the tendon introduces two effects in the beam-tendon system. Firstly, it reduces the natural frequency of the beam-dominated modes due to the effect of the tendon-induced axial force and, secondly, it creates a number of veering regions due to the presence of a number of new, tendon-dominated modes. Both of these findings were also obtained in [17–19], but the latter was not observed in other studies [12–14, 20] where only the former effect was captured while modelling the tendon as an axial force. The study of different tendons highlighted that thicker, heavier tendons produce more vibration modes in the same frequency range. In addition, the rate of frequency increase with the applied tension is lower than for thinner, lighter tendons. Two further numerical studies complemented the experimental validation by showing that the torsional modes are not coupled to the tendon, and the correct prediction of the critical compressive forces is achieved with the proposed model.

A number of assumptions have been considered to derive the governing equations of motion. Most importantly, the Euler-Bernoulli theory was used and the tendon was modelled as a taut string where it was assumed that its diameter remains constant [4]. In order to facilitate the Euler-Bernoulli theory, the transverse shear deformation, rotary inertia effects and the sectional warping of the beam were neglected [1]. The comparison of the theoretical and experimental natural frequencies of the under-lying beam model performed in section 3.2 showed that the error in the theoretical natural frequencies of higher bending modes is more than 5%. Similar errors were observed in other studies about cantilever Euler-Bernoulli beams. For example, in [29] free vibration analysis of aluminium and mild steel cantilever beams with a rectangular cross-section was conducted. It was found that the error between theoretical and experimental natural frequencies is low for the first two modes (about 2%) and much higher (up to 21%) for higher modes. Similarly, in [30] free vibration of beams carrying masses and springs elements was investigated. It was found that regardless of the addition mass and spring, there is an error between the theoretical and experimental natural frequencies that is increasing for higher modes (up to 12% error for the 4^{th} bending mode). The errors observed in this paper and in the previous studies can be attributed to the known limitation of the Euler-Bernoulli theory that overestimates the natural frequencies of higher modes [1, 6, 26].

In the present paper, the beam-tendon system has been studied without any particular application in focus. However, it was suggested in [18, 19, 31, 32] that such a system could be ultimately incorporated in rotorcraft to introduce a means of controlling its dynamics properties. By changing the tension of the tendon, the natural frequencies of rotorcraft blade could be adjusted and this in turn should enable rotorcraft to operate over a wider range of rotor configurations or with variable rotor speed, thereby increasing their efficiency and decreasing their fuel burn, air pollution and noise emission in the future.

6. Conclusion

In this paper, the theoretical model of the beam-tendon system has been derived and thoroughly experimentally validated. It has been found that the natural frequencies vary with the applied tendon tension. While the frequencies of the beam-dominated modes decrease gradually, the frequencies of the tendon-dominated modes increase rapidly. Consequently, many veering regions occur between the beam- and tendon-dominated modes. The numerical and experimental study of the tendon mass also revealed that heavier tendons produce lower natural frequencies with slower rate of increase. Further numerical studies also showed that the tendon has a very little effect on the torsional modes and the structural stability of the system can be correctly predicted.

Acknowledgements

The authors would like to acknowledge the financial support of the European Community's Horizon 2020 Program provided through the project "Shape Adaptive Blades for Rotorcraft Efficiency (SABRE)", Grant Agreement 723491.

References

[1] S. S. Rao, Vibration of Continuous Systems, 2007.
[2] A. Rosen, Structural and dynamic behaviour of pretwisted rods and beams, Applied Mechanics Reviews 44 (12) (1991) 483–515.
[3] D. Hodges, Nonlinear Composite Beam Theory, American Institute of Aeronautics and Astronautics, 2006.
[4] A. H. Nayfeh, P. F. Pai, Linear and Nonlinear Structural Mechanics, Wiley, 2008.
[5] T. Kocatürk, M. Simsek, Vibration of viscoelastic beams subjected to an eccentric compressive force and a concentrated moving harmonic force, Journal of Sound and Vibration 291 (1-2) (2006) 302–322. doi:10.1016/j.jsv.2005.06.024.
[6] M. Rafiee, F. Nitzsche, M. Labrosse, Dynamics, vibration and control of rotating composite beams and blades: A critical review, Thin-Walled Structures 119 (January) (2017) 795–819. doi:10.1016/j.tws.2017.06.018.
[7] L. Virgin, Vibration of Axially-Loaded Structures, Cambridge University Press, 2007.
[8] Z. Bazant, L. Cedolin, Stability of Structures: Elastic, Inelastic, Fracture and Damage Theories, World Scientific, 2010.
[9] S. Timoshenko, J. Gere, Theory of Elastic Stability, Engineering societies monographs, Dover Publications, 1961.
[10] S. Korkmaz, A review of active structural control: challenges for engineering informatics, Computers and Structures 89 (23-24) (2011) 2113–2132. doi:10.1016/j.compstruc.2011.07.010.
[11] A. Preumont, Vibration Control of Active Structures: An Introduction, Springer Netherlands, 2012.
[12] S. Nudehi, R. Mukherjee, S. Shaw, Active vibration control of a flexible beam using a buckling-type end force, Journal of Dynamic Systems, Measurement, and Control 128 (2) (2006) 278. doi:10.1115/1.2192836.
[13] J. Issa, R. Mukherjee, S. Shaw, Vibration suppression in structures using cable actuators, Journal of Vibration and Acoustics 132 (3) (2010) 031006. doi:10.1115/1.4000783.
[14] P. Thomson, G. Balas, P. Leo, The use of shape memory alloys for passive structural damping, Smart Materials and Structures 4 (1) (1995) 36.
[15] G. Cheng, J. W. Zu, Dynamic analysis of an optical fiber coupler in telecommunications, Journal of Sound and Vibration 268 (1) (2003) 15–31. doi:10.1016/S0022-460X(02)01575-4.
[16] D. X. Cao, W. Zhang, Global bifurcations and chaotic dynamics for a string-beam coupled system, Chaos, Solitons and Fractals 37 (3) (2008) 858–875. doi:10.1016/j.chaos.2006.09.072.
[17] J. du Bois, N. Lieven, S. Adhikari, A tensioned cable as an adaptive tuned vibration absorber for response suppression in rotorcraft, in: ISMA 2012 International Conference on Noise and Vibration Engineering, 2012.
[18] V. Ondra, R. Dibble, B. Titurus, Towards an application of an active tendon in rotorcraft: A numerical and experimental study of coupled bending-torsion vibration of a beam-tendon system, in: 28th International Conference on Noise and Vibration engineering (ISMA 2018), 2018, pp. 3645–3659.
[19] R. Dibble, B. Titurus, Helicopter rotor blade modal tuning using internal preloads, in: International Seminar on Modal analysis (ISMA), 2016.
[20] R. Dibble, V. Ondra, B. Titurus, Resonance avoidance for variable speed rotor blades using an applied compressive load, Aerospace Science and Technology 88 (2019) 222 – 232. doi:10.1016/j.ast.2019.03.009.
[21] J. Kierzenka, L. Shampine, A BVP solver based on residual control and the Matlab PSE, ACM Transactions on Mathematical Software 27 (3) (2001) 299–316. doi:10.1145/502800.502801.
[22] J. Bendat, A. Piersol, Random Data: Analysis and Measurement Procedures, John Wiley & Sons, Inc., 2000.
[23] B. Peeters, H. Van Der Auweraer, P. Guillaume, J. Leuridan, The PolyMAX frequency-domain method: a new standard for modal parameter estimation?, Shock and Vibration 11 (2004) 395–409. doi:10.1155/2004/523692.
[24] J. Arora, Introduction to Optimum Design, Academic Press, 2011.
[25] D. J. Ewins, Modal Testing: Theory, Practice and Application, Research studies press Ltd, 2000.
[26] S. M. Han, H. Benaroya, T. Wei, Dynamics of transversely vibrating beam using four engineering theories, Journal of Sound and Vibration 225 (5) (1999) 935 – 988. doi:doi.org/10.1006/jsvi.1999.2257.
[27] N. C. Perkins, C. D. Mote, Comments on curve veering in eigenvalue problems, Journal of Sound and Vibration 106 (3) (1986) 451–463. doi:10.1016/0022-460X(86)90191-4.
[28] B. R. Mace, E. Manconi, Wave motion and dispersion phenomena: Veering, locking and strong coupling effects, The Journal of the Acoustical Society of America 131 (2) (2012) 1015–1028. doi:10.1121/1.3672647.
[29] S. W. Prashant, V. Chougule, A. C. Mitra, Investigation on modal parameters of rectangular cantilever beam using experimental modal analysis, Materials Today: Proceedings 2 (4) (2015) 2121 – 2130, 4th International Conference on Materials Processing and Characterzation. doi:doi.org/10.1016/j.matpr.2015.07.214.
[30] Z. Wang, M. Hong, J. Xu, H. Cui, Analytical and experimental study of free vibration of beams carrying multiple masses and springs, Journal of Marine Science and Application 13 (1) (2014) 32–40. doi:10.1007/s11804-014-1231-4.
[31] V. Ondra, R. P. Dibble, B. Titurus, B. K. S. Woods, An active tendon concept in rotorcraft with variable speed rotors: free vibration perspective, in: AIAA Scitech 2019, no. January, 2019, pp. 1–14. doi:10.2514/6.2019-0857.
[32] J. Rauleder, B. G. van der Wall, A. Abdelmoula, D. Komp, S. Kumar, V. Ondra, B. Titurus, B. K. S. Woods, Aerodynamic Performance of Morphing Blades and Rotor Systems, in: AHS International 74th Annual Forum & Technology Display, Phoenix, Arizona, USA, 2018.